Contents lists available at ScienceDirect

International Journal of Adhesion & Adhesives

Adhesively bonded lap joints with extreme interface geometry

Babak Haghpanah, Shihung Chiu, Ashkan Vaziri *

Department of Mechanical and Industrial Engineering, Northeastern University, Boston, MA 02115, United States

ABSTRACT

The role of adhesive–adherend interface morphology (through intentional deviation from a flat joint plane) on the mechanical behavior of adhesively bonded lap joints is studied. Two mirror-image types of joints with a zigzag interface containing 'positive and negative' interlocking teeth were fabricated and their tensile behavior was measured and compared to the response of a standard flat joint. Numerical simulations were used to explore the role of tooth height and width on the stress distribution in the adhesive, and on crack propagation and arrest after initial fracture. The data suggest that stress distribution along the bond line – and thus, the initial fracture load of the joint – is altered considerably by the positive and negative interlocking teeth. The tendency of a crack to either propagate along the bond or to arrest also depends strongly on morphological details. When crack arrests, the bonded joint can sustain a higher load and thus benefits from some of the intrinsic properties of the adherends (e.g. the plasticity of metal adherends) to enhance energy absorption and toughness. Our findings provide insight for the development of robust multi-material and multi-component structural systems with tailorable properties, and for understanding the role of interface morphology in some biological systems.

© 2013 Elsevier Ltd. All rights reserved.

1. Introduction

Where structural materials join together, geometrical or elastic discontinuities generally lead to a complex state of deformation and concentrated stresses, which may encourage cracks and defects to initiate and propagate along the bonded joint. The challenge of joint design is especially pronounced for non-metallic structures, since traditional ductile attachment techniques (e.g., welding or brazing) cannot generally be employed. Adhesive properties have been shown to be the limiting factor in many bonded systems [1–4]. This has stimulated the development of better adhesives [5–9] and surface treatments which modify the micro-topography of the adherend surfaces [1,2,10,11]. Another promising avenue for enhancing bond properties is to tailor the joint geometry (by adherend scarfing or tapering, adhesive fillets, etc.) [5,12,13]. For example, bonded wavy lap joints exhibit higher strength than a counterpart flat lap joint [14–17]. Here, we extend these studies by introducing extreme morphological changes close to the edges of bonded lap joints, where peel and shear stresses are known to be intensified [18–23]. It was hypothesized that strength and ductility could both be enhanced by changing the bonded region topography.

The challenge of creating joints with elevated strength and ductility has been well addressed in nature, where the connections

between organic and inorganic materials generally occur at multiple length scales. An example is nacre (mother-of-pearl), a natural nano-composite of ceramic and biopolymer with surprising mechanical properties [24–26]. The toughness of nacre [24] is partly attributed to interlocking 'wave shape' polygon tablets, which delay localization by propagating deformation through the entire structure [25–29]. The roles of geometrical organization and topology on improving the behavior of materials and structures have also been demonstrated in other biological systems. For example, the heterogeneous structural organization of bone is shown to be critical for its superb energy dissipation and toughness [30,31].

Geometrical and structural organizations have been also exploited recently to develop high-performance *multifunctional* materials and structural systems. Hierarchical honeycombs [32–34] and functionally graded cellular structures [35,36] are examples of such developments, which can be tuned to exhibit enhanced properties. Another unique example is the recent demonstration of *Buckliballs*, a class of patterned shells that undergo large buckling-induced deformations under pressure, of a type not observed in continuum shells [37].

Our study includes fabricating and testing bonded lap joints with different interface morphologies, along with detailed finite element modeling. For our experiments (Section 2), we fabricated standard flat joints as well as joints with two mirror-image zigzag surface morphologies, and measured the tensile behavior up to failure. The experiments themselves were not intended to explore extensive parameter variations, but rather to benchmark and

validate the associated finite element (FE) modeling. It was observed that each kind of non-flat interface morphology displays a characteristic and explainable load–displacement curve, with an initial cracking or debonding event, followed by rapid crack propagation or arrest depending on the interface morphology. A particular geometry was identified as offering twofold to threefold reduction in maximum peel stress over the experimentally evaluated non-flat geometries, and thus by implication, greater initial failure strength than the standard flat lap joint. In Section 3, linear-elastic FE analysis using ABAQUS is employed to evaluate distributions of stress and strain in all the experimental geometries. Also FE simulations are used to obtain the optimized geometrical parameters resulting in the largest strength and load capacity. In Section 4, we carried out further simulations to study elastic stresses in joints with partially debonded lengths. The results can provide insight into bonded-joint crack propagation, thus revealing the behavior after initial cracking. Conclusions are presented in Section 5.

2. Experimental investigation

2.1. Specimen preparation and test methods

Adherends with three different profiles were machined from 1018 CR steel bar with the following assumed properties:

Young's modulus, $E_s = 200$ GPa, Poisson ratio 0.3, and tensile yield strength 386 MPa. The adherends' length d, width w, and mean height h were 120 mm, 3 mm, and 10 mm, respectively. Standard flat lap joints, as well as two non-flat types with a v-shaped tooth and the matching v-shaped notch (or negative tooth) on each adherend were fabricated and tested. The two non-flat types of adherends are as follows:

- "Positive then negative tooth" adherend defined by each adherend becoming thicker (i.e., a tooth) as it enters the joint region from its grip. This morphology is frequently denoted by '/\' or 'first point upward' in the paper.
- "Negative then positive tooth" adherend defined by each adherend becoming thinner (i.e. a notch) as it enters the joint region from its grip. This morphology is frequently denoted by '\/' or 'first point downward' in the paper.

Fig. 1A provides a generic description of joint geometry. Interface morphology is defined by an overlap distance L (the projected bond length), first-tooth slope angle θ, and tooth height A (from which is derivable total tooth width $B = 4A/\tan(\theta)$). Then flat, /\, and \/ joints correspond to θ & $A = 0$; θ & $A > 0$; and θ & $A < 0$, respectively. Each tooth is in the form of an isosceles triangle. We define the geometry in non-dimensional terms through the tooth height to adherend height ratio (A/h), the total tooth width to
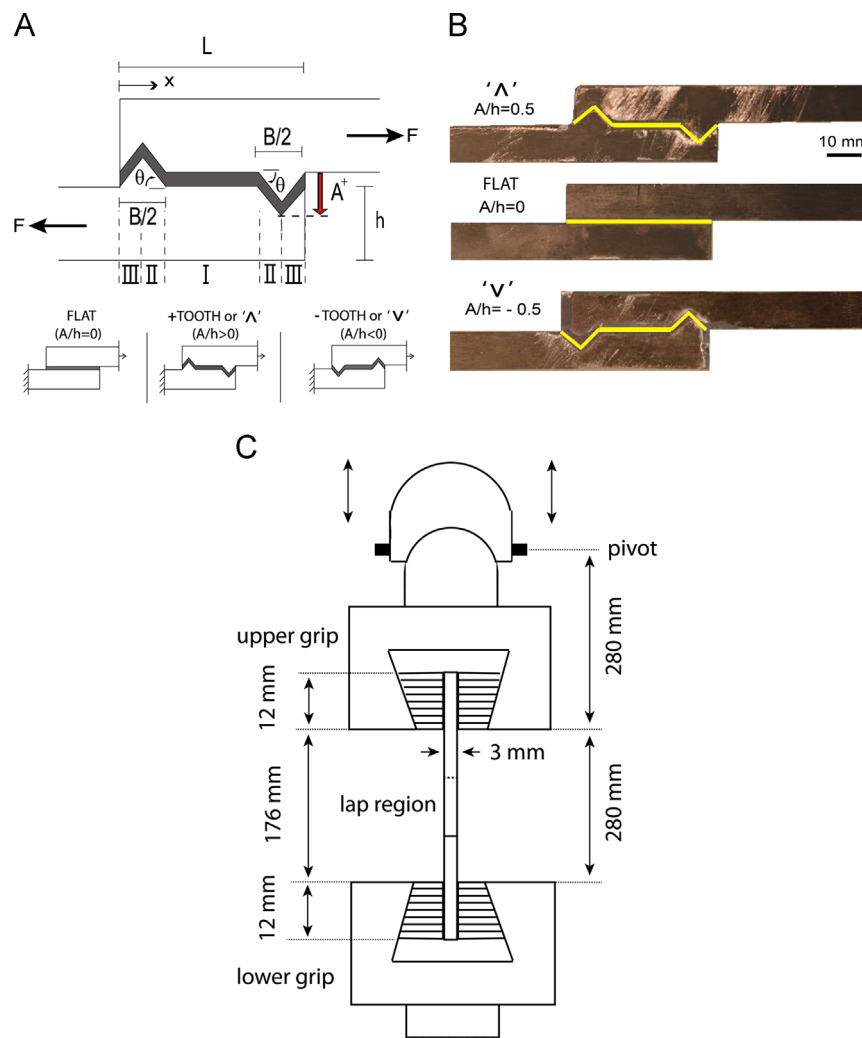

Fig. 1. (A) Schematic of the bonded joint. (B) Bonded joint with three different interface profiles of $A/h = 0.5$, 0 and -0.5. The adherends are made of steel and the adhesive layer is highlighted by lines to better show the interface morphology. (C) Schematic of the experimental setup.

total overlap distance ratio (B/L), and the initial angle (θ) of the joint surface. When teeth are present, the outer tooth flanks, the inner flanks, and the flat between them are named regions III, II and I respectively, as shown in Fig. 1A.

To fabricate the specimens, pairs of matching adherend types were bonded together using Emerson & Cuming "ECCOBOND G909" adhesive. This is a one-component (no mixing required) heat-curing epoxy with excellent peel strength, and high tensile and shear strengths, designed for metal assemblies such as copper and aluminum. The cured adhesive has Young's modulus, $E = 2$ GPa (the manufacturer's value was confirmed by uniaxial test of an adhesive bar), Poisson ratio 0.4, and a nominal bond thickness of 1 mm. The adherends overlapped by $L = 40$ mm, leading to an overall bonded-specimen length of 200 mm.

The adherends were machined to fit together with essentially no gaps, then were separated by 1.0 mm to provide clearance for the adhesive. (Depending on local bond-surface angle θ, the epoxy thickness was thus equal to $(1.0$ mm$) \times \cos \theta$.) The surfaces to be bonded were alcohol-cleaned prior to assembly in a bonding jig. Following supplier instructions, the specimens were cured in an oven for 20 min at 150 °C, then post-cured at room temperature for 2 h. The unwanted residual adhesive on the specimen was removed carefully by grinding, creating a bond-end adhesive fillet radius of approximately 0.8 mm in the re-entrant corners.

A total of 21 specimens – 7 for each interface type illustrated in Fig. 1A – were fabricated and tested. The specimens with non-flat geometries had $B/L = 0.5$ (total tooth width being half the 40 mm specimen overlap). For '/\' morphology, $A/h = 0.5$ (a tooth protruding 5 mm from the adherend where it begins the overlap), while for '\/' morphology, $A/h = -0.5$ (a 'negative tooth' or notch with

adherend material removed to a depth of 5 mm). The angles θ in the two cases are $\pm 45°$. Enlarged illustrations of the three joint types are shown in Fig. 1B.

Uniaxial tensile tests were performed on an INSTRON 5582 universal testing machine at a displacement rate of 1 mm/min. For the tensile test, approximately 12 mm at each end was gripped, leaving 176 mm between testing grips. Fig. 1C shows the schematic of the experimental setup. One rigid grip, and one self-aligning grip with its pivot 280 mm from the grip face, contacted the specimens on the 10 mm wide faces visible in the figures (not the 3 mm 'top and bottom' faces). Since only one of the grips was self-aligning, the load's line of action would be expected to deviate slightly from the bond plane due to elastic asymmetry (the elastic principal axis is not quite vertical). Developing cracks were monitored using imaging by cameras place on two sides of the specimen. There was no evidence of axial twist (in the plane normal to the adherends length) in the bonded joints.

Two separate sets of experiments were also performed to assess the strength of the cured adhesive material and adhesive–adherend interface under uniaxial tensile loading. In the first experiment, uniform bars of cured adhesive were made using the aforementioned procedure, and subjected to tension. The fracture type was a brittle cleavage with no apparent sign of plastic deformation in a plane almost normal to the loading direction. In the second set of experiments, pairs of aluminum bars with square cross section were bonded together by the adhesive from the smallest cross section (i.e. the ends) and were subjected to a uniaxial tensile loading. The results showed that failure due to normal stress in a case of high triaxiality occurs at the adherend–adhesive interface (i.e. adhesive failure) rather than
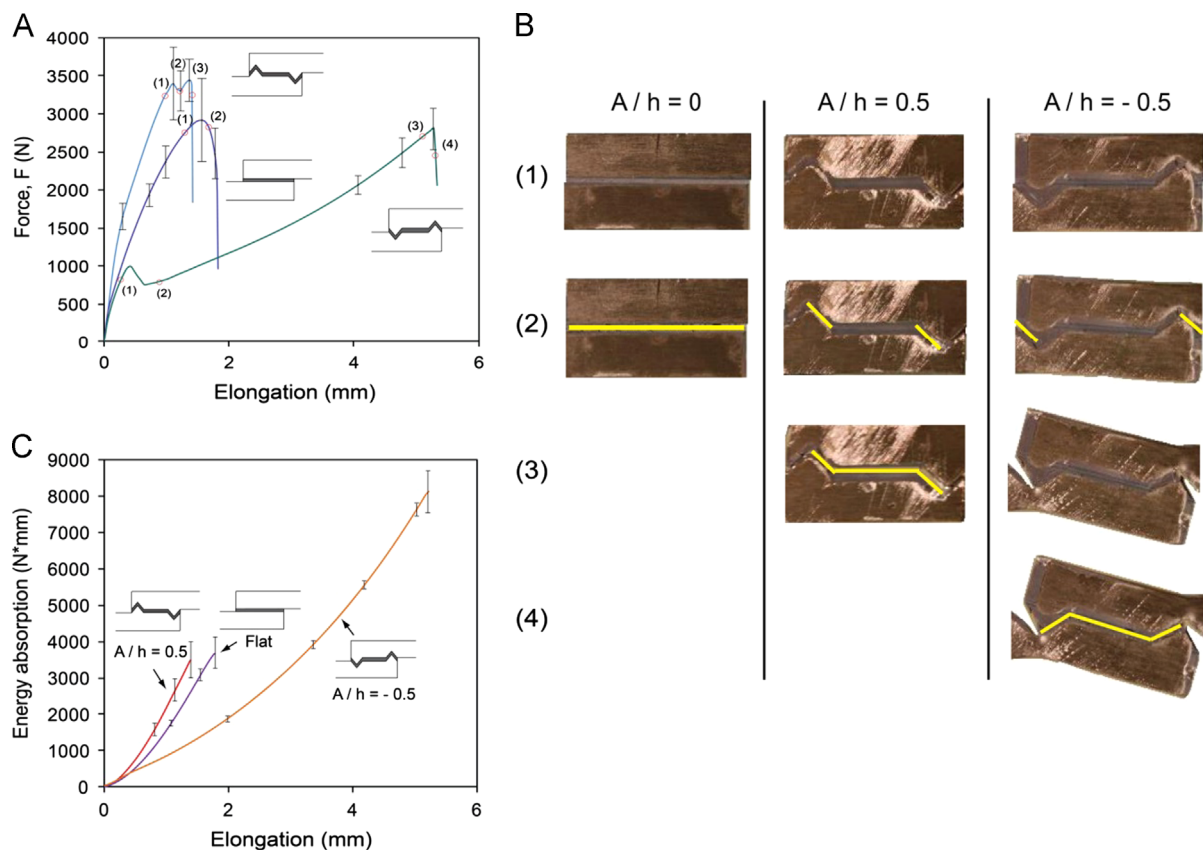

Fig. 2. (A) Force–elongation response of three bonded joints with $A/h = 0.5$, 0, -0.5. (B) The deformed configuration of specimens at different stages of the experiments annotated with numbered 'events' in A. Here, the lines show the failed interface regions at each stage of deformation. (C) Dissipated energy versus elongation for different specimens, calculated based on the response shown in A.

within the bulk adhesive (i.e. cohesive failure). The tensile strength of the adherend–adhesive interface was estimated ~54 MPa from this set of experiments.

2.2. Experimental results

Fig. 2A shows measured applied-force versus elongation results. Each curve represents a typical response for each specimen type, with range bars indicating the greatest and least load measured at specific elongations. The curves are annotated with numbers denoting images of the typical specimen at each stage of loading (Fig. 2B). The light lines added to the images show the failed regions at each stage of deformation.

Clearly, the three types of joint differ significantly in their mechanical response. For the non-flat specimens, the 'first bond failure' (indicated as stage 2) probably occurs due to normal stress across the adhesive bond, as will be further discussed in Section 3. For the '/\' specimens, the initial crack development occurs almost simultaneously in the pair of regions II (as shown in Fig. 2B) at a load of approximately 3300 N (corresponding to far-field adherend tensile stress of 110 MPa). However for '\/' specimens, the initial cracks develop at the adherend–adhesive interface at the outer edges of the bond (i.e., regions III), at a load around 800 N. For comparison, flat-joint ultimate strength is approximately 2900 N, implying an average shear strength of 24 MPa.

After initial failure in non-flat joints, the specimen types respond differently to further elongation. For '/\' specimens, after the initial occurrence of cracks in regions II, propagation is slightly delayed by the change of interface slope between regions II and I. This results in a slight increase in the load resistance of the specimen, which may be identified by a second distinct peak in the load–displacement response, Fig. 2A. Directly after this second peak the two initial cracks in regions II link up in region I, overload the remaining bonded regions III and cause sudden specimen breakage.

For '\/' specimens, the initial cracks develop and propagate quickly at very low loads in regions III of the bonded interface, causing a small drop in the associated force–displacement curve (compare negative tooth photos 1 and 2 in Fig. 2B). However, the cracks arrest at the tooth tips connecting regions III and II, and no crack growth is observed for a relatively large span of further loading (i.e. between images 2 and 3). During this stage of loading, the region III cracks open further, and plastic hinges form in the thinnest section of each adherend, as seen in Fig. 2B images (3) and (4). The relatively large amount of work to failure is primarily due to localized plastic bending of the adherends, as region I rotates to bring the plastic hinges closer to the line of the load. At stage (4) the cracks from both right and left ends of the joint connect in regions I and II, causing complete separation. It may be noted that essentially the same behavior would be expected if no adhesive were placed in regions III. In other words, the end segments of the '\/' bond appear to be insignificant to the load capacity and response, and could perhaps be dispensed with in order to eliminate the initial failure stage and associated drop in load.

In the next sections, it will be seen that the 'initial cracking' events of non-flat bonds are reasonably predicted by FE analysis. Subsequent FE-based explorations on various geometrical parameters revealed joints for which this initial failure strength is predicted to be significantly higher than the tested non-flat cases (i.e. $A / h = \pm 0.5$ and $B / L = 0.5$).

The failure sequence for flat-joint specimens is less clear. The adhesive undergoes very substantial inelastic shear strain (1.5 mm elongation of a specimen with 1 mm thick adhesive layer), and then develops distributed cracking (approximately perpendicular to the largest adhesive principal strain) rather than interface separation. It appears that the elastic analysis and measurement of adhesive bond strength are not helpful in predicting flat joint failure, which could be due to a maximum tensile strain criterion. The effect of bond failure in non-flat joints is further explored in Section 4, where the stress distribution in the adhesive is estimated using finite element simulations.

Another important aspect of behavior is energy absorption. Considering the overall behavior of bonded joints, flat and '/\' specimens show somewhat less-tough macroscopic behavior, where the occurrence of initial cracking is followed rapidly by overall breakage and sudden loss of load carrying capacity. In contrast, the response of '\/' specimens resembles the *ductile* behavior of most metals, where initial failure causes only a slight reduction in resisting force of the bonded joint. Further elongation results in an increase in load-carrying capacity of the specimen up to the point of failure. In fact, the overall response of '\/' specimens after the initial cracking is regulated by plastic hinges in the metallic adherends at the points of minimum cross section, leading to significant rotation of the bonded region prior to overall breakage. (In contrast, the stresses in the metallic adherends of the flat and '/\' specimens never reach yield.)

To further illustrate the different between the responses, in Fig. 2C we have plotted the mechanical energy absorbed by each specimen, calculated from the area under the force–elongation curves shown in Fig. 2A. It should be noted that the energy absorbed by the specimen in the early stages of deformation is mainly due to elastic deformation, and is recovered if the specimen is unloaded. For '/\' specimens, energy is dissipated as the crack propagates through the bond interface and adhesive layer deforms. For '\/' specimens, the initial elastic regime is followed by plastic dissipation at the adherend plastic hinges, and final cracking of the interface. For the flat specimens, energy is dissipated in plastic work of the adhesive, ending in distributed cracking.

3. Finite element simulations

3.1. Finite element model

Computational analysis of single-lap adhesively bonded joints was performed using the FE analysis software ABAQUS. Adherends and adhesives were modeled as homogeneous isotropic linear elastic materials, with properties given in Section 2. No failure criteria were incorporated in the analysis, but computed average peel stress normal to adhesive–adherend interface was used to predict the experimental failure initiation (i.e. cracking) due to brittle failure of the cured adhesive material. Eight-node plane stress elements with reduced integration (two degrees of freedom at each node and quadratic shape functions) were used for meshing. The adhesive layer was meshed with ten elements through its height of 1 mm. In contrast, the much thicker adherends were meshed with about 12 elements through the height of 10 mm, transitioning from 2 mm at the outer edges to 0.1 mm at the adhesive–adherend interface. To allow averaging of nodal results over adhesive thickness, nodes at the adhesive upper surface have the same x-coordinates as nodes at the adhesive lower surface but y-coordinates that are greater by 1 mm (with x and y being the horizontal and vertical axes, respectively).

One end of the modeled specimen was fixed (clamped boundary condition), while the other end was constrained to translate axially with fixed slope parallel to the bond plane, and loaded with an axial force F. Unlike the experimental loading with one self-aligning grip, the rotation-suppressed loading in ABAQUS imposes a net normal (i.e., peeling) load on the joint of order $\sim Fh/(d - L/2)$. (This beam-theory estimate arises by considering the clamped adherend as a cantilever, with the bond center point
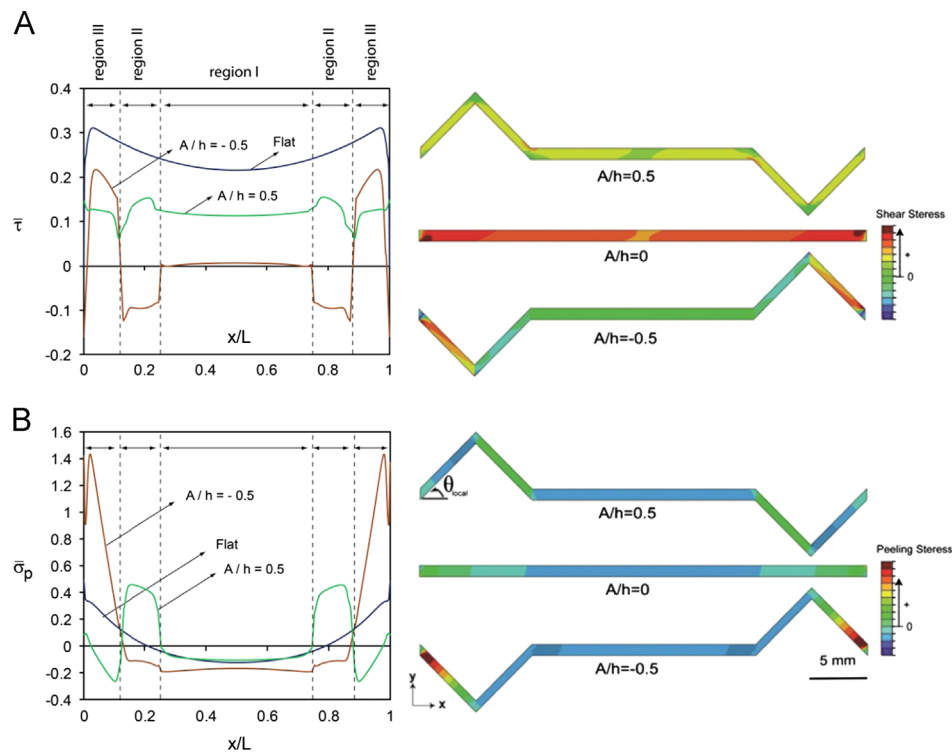
Fig. 3. Normalized shear stress (A) and peel stress (B) versus normalized overlap length, x/L, for models with $A/h=0.5$, 0 (flat) and -0.5. The distributions of shear and peel stress in the adhesive layer are also plotted for each case. The results are presented for $E/E_s = 0.01$, which corresponds to the experiments.

undergoing zero transverse displacement by anti-symmetry. The cantilever is subjected to a uniform bending moment of approximately $Fh/2$ due to the line of action of the load, along with a simultaneous transverse load to be found by the condition of zero lateral displacement).

In the numerical simulations, the total overlap length L of the bond, total specimen length $2d-L$, height h of the specimen, and thickness t of the adhesive were kept constant. Varied quantities included geometric parameters such as tooth height and width, adhesive Young's modulus (Section 3), and length of sections of interface with no bonding to simulate existence of crack (Section 4).

The finite element analysis provides an estimate of the elastic stress distribution in the bonded joint. As one way to estimate peel (i.e., normal) and shear stresses in the adhesive, computed stress components at corresponding upper and lower adhesive boundary mesh points are averaged to give 'mean adhesive layer stresses': σ_{xx}, σ_{yy} and σ_{xy}. These were used to calculate adhesive layer average peel and shear stresses, denoted by σ_p and τ, respectively, according to:

$$\sigma_p = \sigma_{xx}\sin^2\theta + \sigma_{yy}\cos^2\theta - 2\sigma_{xy}\sin\theta\cos\theta$$

$$\tau = -(\sigma_{xx}-\sigma_{yy})\sin\theta\cos\theta + \sigma_{xy}(\cos^2\theta - \sin^2\theta)$$

where θ is the angle of the adhesive layer at a given section as shown in Fig. 1A ($\theta=0$ denotes a flat region in the interface). These computed stress results were normalized by the applied far-field adherend tensile stress, and presented in non-dimensional form as $\overline{\sigma}$ and $\overline{\tau}$, respectively.

3.2. Finite element results

In the first set of calculations, only the three specific experimental geometries ($A/h=0.5$, 0, -0.5) were simulated. For each, the averaged shearing stress (tangential to the adhesive–adherend interface) and peeling stress (normal to the interface) were obtained all along

the bonded joint, as shown in Fig. 3A and B, respectively. In this set of calculations, the adhesive Young's modulus was 2 GPa ($E/E_s = 0.01$), just as for the experimental results. The results are presented in terms of the non-dimensional quantities $\overline{\sigma}$ and $\overline{\tau}$, as discussed above. The spatial distributions of non-averaged shear and peel stresses within the adhesive are also plotted. This reveals that the elastic stress distribution in the adhesive layer is substantially different in the three specimens, being strongly affected by interface slope and slope discontinuities.

In both non-flat cases, the maximum tensile peel stress is significantly higher than the maximum shear stress. For models with $A/h=0.5$, the maximum tensile peel stress of 0.45 times the remote tensile stress occurs in regions II, where the initial cracking was observed in our experiments. Peel stress in region III is mainly compressive, so failure is not expected to initiate in this region. The initial failure of such specimens around 3300 N suggests peel strength of 49 MPa. This estimate is in a good agreement with the estimate of 54 MPa from tensile experiment of adhesively connected bars (Section 2.1). The maximum tensile peel stress in the model with $A/h=-0.5$ occurs in regions III at intensity approximately 1.43 times the remote tensile stress, and the initial failure of such specimens occurs around 800 N. As observed in the experiments, this initial failure will result in a drop in the associated load–displacement curve but not the complete loss of load bearing capacity of the joint.

Since these two kinds of specimen display substantially different strengths and failed at similar values of peak computed peel stress, in the next section we provisionally adopted computed peak peel stress as a failure criterion, in order to predict the strength of other geometries.

3.3. Results of parametric explorations

To understand the effect of joint parameters on the distribution of stresses throughout the adhesive on the performance and load capacity of non-flat bonded joints, we carried out an extensive
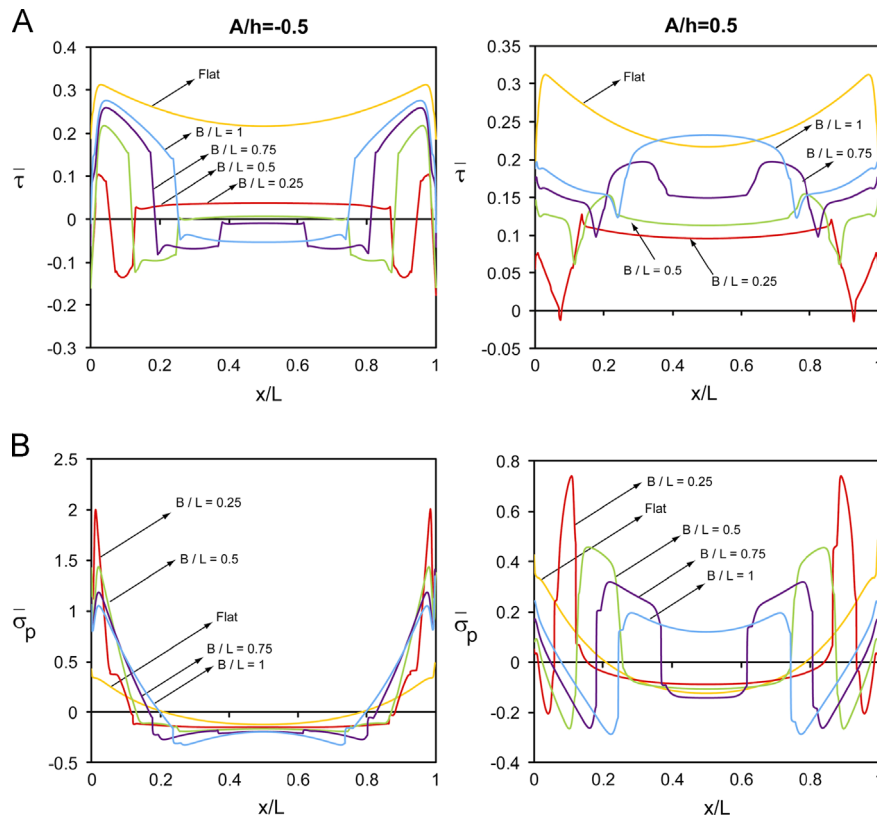
Fig. 4. The distributions of shear (A) and peel (B) stress in adhesive layers with different morphologies. The results for joints with $A / h = -0.5$ and 0.5 are presented in left and right plots, respectively. In each plot, the stress distributions are plotted for joints with various ratios of total tooth width to total projected bond length, $B / L = 0$, 0.25, 0.5, 0.75, 1.

parametric study. Fig. 4 shows the distribution of normalized shear (A) and peel (B) stress along the projected adhesive path for non-flat joints with various ratios of total tooth width to total projected bond length, B / L, and tooth height to adherend height ratios of $A/h = -0.5$ and 0.5. The stresses are normalized by the far-field adherend tensile stress. Results for the flat joint are plotted for comparison. Stresses vary only gently in the flat regions of all bonded joints. The non-flat joints have lower maximum shear stresses compared to the flat joint, with the lowest maximum shear stress occurring for the joint with $B/L = 0.25$. The peak shear stress, however, is expected to have relatively little effect on the initial failure load of these joints. The peel stress distribution varies significantly for both sets of non-flat bonded joints, showing smaller values for the bonded joints with positive A / h. The maximum peel stress for the joints with $A/h = -0.5$ occurs in region III and is the highest for the joint with $B/L = 0.25$. However, for the joints with $A/h = 0.5$, peel stress maxima are found at the edges of the joints as well as in region II. For the joints with $B/L = 0.25$, 0.5 and 0.75, the maximum peel stress occurs in region II. Only when $B/L = 1$ is the peel stress at the end slightly higher that the peel stress in region II.

We next explored the role of tooth height on the stress distribution in non-flat bonded joints. Fig. 5 shows the effect of A / h on the maximum value of normalized peel stress in the bonded joint with $B/L = 0.5$. Two values of adhesive Young's modulus were considered, namely the experimental 2 GPa ($E/E_s = 0.01$) and a hypothetical 0.8 GPa ($E / E_s = 0.004$). The shear stress results are not presented, since they are usually significantly lower than the peel stress values, and it is unlikely that shear stress peaks lead to failure. The plotted results were obtained by calculating the elastic stress distribution for individual bonded joint configurations and finding the maximum tensile

(positive) peel stress along the bond line. Compressive peel stresses are unlikely to cause cracking and failure and are not considered here. In this plot, the solid lines show the maximum peel stress along the bonded joint and the dashed lines show the maximum peel stress in the outer regions (i.e. regions III). For negative values of A / h, the maximum peel stress occurs in region III, as was discussed previously in Figs. 3 and 4, and thus the dashed lines and solid lines coincide in this section of the plot. However for positive values of A / h, the dashed lines shown that the outer regions (III) experience a lower peak peel stress, explaining why failure started in region II in our experiments (Section 2). In addition, the lower-modulus adhesive has somewhat decreased peel stress for negative values of A / h. However, for joints with positive A / h, the maximum peel stress is almost unaffected by adhesive elastic modulus. The rest of the results discussed below focus on the role of interface morphology and more specifically tooth width and height on the stress distribution along the bonded joint. In this set of calculations, the adhesive Young's modulus was 2 GPa ($E / E_s = 0.01$), just as for the experimental results.

Fig. 6 is a plot of the maximum peel stress as a function of A/h for bonded joints with various ratios of total tooth width to total projected bond length, B / L. Increasing the tooth width generally leads to smaller values of maximum peel stress in the bonded joint. For negative A / h, the curve for $B/L = 1$ is the lowest, and in fact having no 'flat' area guarantees low peel stress in general. The specific case exhibiting the very lowest peak peel stress is a triangle at $B/L = 0.75$ and $A/h = 0.5$ (so $\theta = 33.7°$), with a peak normalized peel stress of about 0.17, which is less than 35% that of the experimental '/\' specimens with $A/h = 0.5$ and $B/L = 0.5$. Such a geometry should exhibit an estimated threefold of improvement in initial failure strength over the strongest experimentally tested
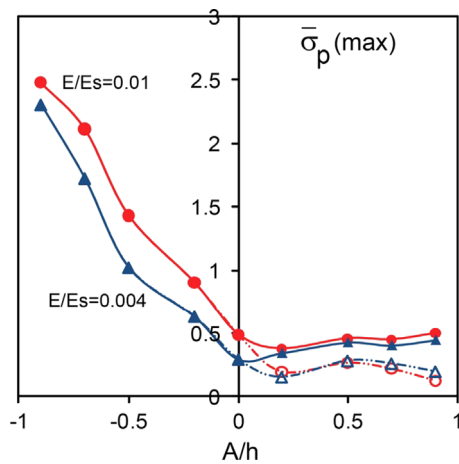
Fig. 5. Normalized maximum peel stress in the bonded joint versus A/h for two adhesive normalized Young's modulus $E/E_s = 0.01$ and 0.004. The solid lines show the maximum peel stress along the bonded joint and the dashed lines show the maximum peel stress in the outer regions (regions III). In this set of calculations, $B/L = 0.5$.
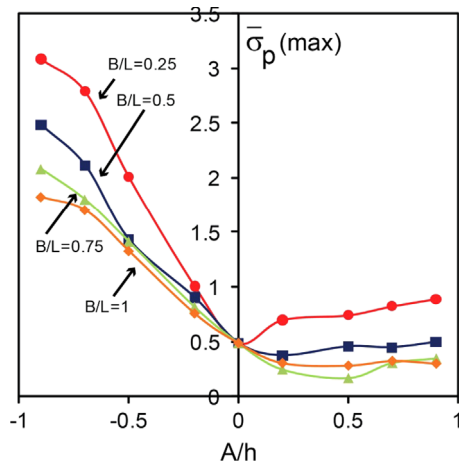

Fig. 6. Normalized maximum peel stress in the bonded joint versus A/h for joints with different total tooth width to total projected bond length, B/L. In this set of calculations, $E/E_s = 0.01$.

specimens (i.e. $A/h = B/L = 0.5$). Note that the 'initial cracking' events observed in the experimentally tested joints (i.e. $A/h = \pm 0.5$ and $B/L = 0.5$) can be reasonably predicted by the finite element maximum peel stress results that are presented in Fig. 6. Therefore, although the experimentally evaluated non-flat specimen geometries did not exhibit substantial improvement in ultimate joint strength, the finite element results demonstrate that interface morphology has a significant influence on the overall behavior and suggest that certain non-flat geometries could be significantly stronger.

Based on the results presented above, we can see that, in general, increasing the B/L value or decreasing the absolute value of A/h in the negative region result in the same trend of decreasing stress, and recognize that both of these changes also decrease θ. In Fig. 7, we have replotted all results for normalized maximum peel and shear stress against θ. The data are presented for joints with four different non-dimensional tooth widths $B/L = 0.25$, 0.5, 0.75 and different amplitudes, representing a wide range of values for tooth angle, θ. Evidently, angle θ is the primary determinant of peak stresses in the bonded joint. The dashed lines in Fig. 7 show the best fit to the data points shown. These lines can be used for estimating the values of maximum stresses in non-flat joint with different configurations. From the results, it can be
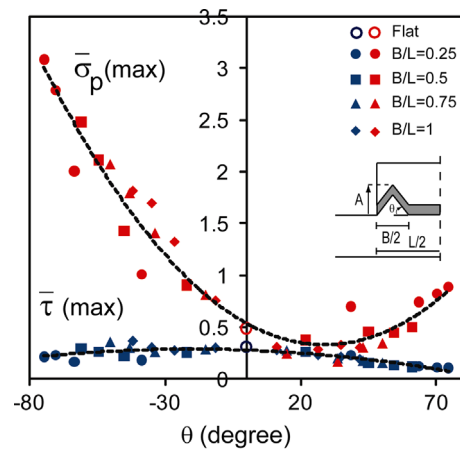

Fig. 7. Normalized maximum shear and peel stress at adhesive versus the starting angle θ for different geometry ratios $B/L = 0$, 0.25, 0.5, 0.75, 1.

surmised that a θ value between 10 and 35 degrees leads to small stresses and thus, could be a good design choice. It is noteworthy that the results presented here are for bonded joints subjected to uniaxial tension. However, the significant role of interface morphology on regulating the stress distribution along the bonded joints observed here should be valid for other loading conditions and pertinent to other bonded joint configurations and designs (e.g. double lap joint).

4. Stress distribution in the presence of propagating interface cracks

To investigate the behavior of bonded joints after initial cracking, we carried out a separate set of simulations to study the role of a crack on the stress distribution in the bonded joint. In this set of finite element simulations, the three specimen types with previously defined geometries were considered to contain a pair of cracks of length $c/2$ along the adhesive–adherend interface at both ends of the joint, as shown schematically in Fig. 8A. Cracking was modeled by changing the adhesive–adherend contact properties of the cracked sections from bonded, to a frictionless separable contact condition. In this model, the crack region opens up rather than sustaining normal tension. If the cracked region is under normal compression, the crack remains closed and will transfer normal stress, but not shear. Fig. 8B and C shows the peak shear and peel stresses in the bonded joint with different normalized crack length, c/L, respectively. One evident trend in Fig. 8B is the reduction in maximum peel stress with $A/h = -0.5$ after the crack passes the tooth 'peak' and begins to descend (in region II). This correlates well with the observed initial cracking at small loads in experimental trials, followed by arrest at the tooth tips and the significant energy absorption by bending of the adherend at the negative tooth cross section. The plastic deformation in type III steel adherends after initial cracking is ignored in the FE modeling. The FE model also represents the initial cracking of flat and '/\' joints, where the crack initiates at the edge of the joint and then quickly propagates along the joint interface, as discussed in the experimental results.

5. Conclusions

The effects of interface morphology on inelastic elongation, crack initiation and arrest, and energy absorption of geometrically different adhesively bonded single lap joints were investigated
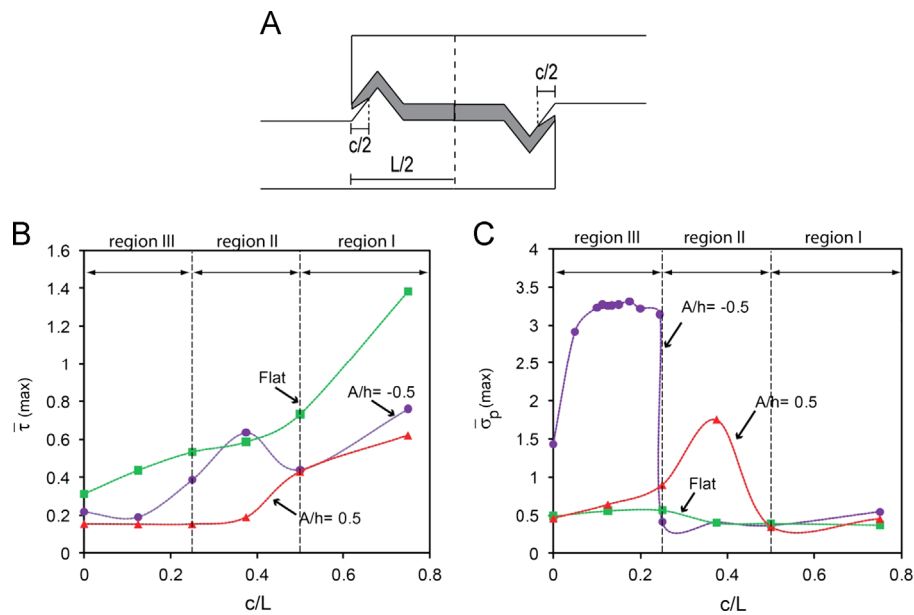
Fig. 8. (A) Schematic of crack in the bonded joint. In this set of finite element simulations, the three different specimen geometries were explored, with cracks of length $c / 2$ growing along the adhesive–adherend interface from both ends. (B) and (C) Normalized maximum shear and peel stresses, respectively, in the joints versus normalized crack length c / L.

experimentally. From the experimental results, bonds that were flat and those with adherends that thickened (positive tooth) as they entered the bond region had approximately similar strengths for initial cracking, while bonds whose adherends thinned (negative tooth) were considerably weaker. However when ultimate strength was considered, all three experimental geometries were similar. The total inelastic elongation of negative-tooth bond morphologies was almost triple that of flat or positive tooth joints, while the energy absorption was more than double. This can be attributed to ductile deformation of the steel adherends. Possibly such enhanced ductility could also be achieved in flat or positive tooth specimens by properly designed notches outside the bond zone, to similarly permit rotation of the bonded region. The observed pattern of strength would be also expected from a consideration of joint stiffness in the stress transfer zone. As a general principle, reducing stiffness at a geometrical discontinuity reduces the stress concentration. In the case of geometrically modified lap joints, the positive tooth geometry is analogous to removing material from the end of an adherend in order to make it more compliant under loading-induced deformation.

FE analysis was used first to understand the initial cracking and initial peak load observed experimentally. The calculated maximum peel stress of an intact (i.e. without any cracks in the FE model) non-flat joint correlated reasonably well with initial cracking observations. FE analysis was then used to explore parameter variations by changing such quantities as tooth height, slope angle, and adhesive modulus while holding fixed the adherend height, adhesive thickness, and bond length. The results from the finite element analysis were able to show that cracks in negative tooth specimens should form on the outermost tooth flanks and arrest when reaching the tooth peaks, as was observed experimentally. An intriguing FE result was prediction of a three-fold stronger positive-tooth geometry for resisting initial cracking, with $B/L=0.75$ and $A/h=0.5$. Another promising avenue for future investigation is a modified negative-tooth joint geometry with no adhesive on the initial tooth flank. It appears that lap joint strength and ductility might both be enhanced by exploiting interface morphology. This would be attempted by using a geometry shown to resist initial cracking, plus adherend notches to increase elongation. The results presented in the current study

are limited to adhesives that exhibit a clear brittle behavior. If a quasi-brittle behavior is assumed for the adhesive material, the stress distribution along the joint interface is affected by the fracture process zone, and a non-linear fracture mechanics concept is necessary for analysis.

References

[1] Davis M, Bond D. Principles and practices of adhesive bonded structural joints and repairs. International Journal of Adhesion and Adhesives 1999;19 (2):91–105.
[2] Kinloch A. Interfacial fracture mechanical aspects of adhesive bonded joints—a review; 1979, 193-219.
[3] Sheppard A, Kelly D, Tong L. A damage zone model for the failure analysis of adhesively bonded joints. International Journal of Adhesion and Adhesives 1998;18(6):385–400.
[4] Xiong J, Ma L, Wu L, Vaziri A. Mechanical behavior and failure of composite pyramidal truss core sandwich columns. Composites Part B: Engineering 2011.
[5] Banea M, Da Silva L. Adhesively bonded joints in composite materials: an overview. Proceedings of the Institution of Mechanical Engineers, Part L: Journal of Materials Design and Applications 2009;223(1):1–18.
[6] Baldan A. Adhesively-bonded joints and repairs in metallic alloys, polymers and composite materials: adhesives, adhesion theories and surface pretreatment. Journal of Materials Science 2004;39(1):1–49.
[7] Wake WC. Synthetic adhesives and sealants. Chichester: Society of Chemical Industry; 1987.
[8] Landrock AH. Adhesives technology handbook. Park Ridge: Noyes Publications; 1985.
[9] Katsiropoulos CV, Chamos AN, Tserpes KI, Pantelakis SG. Fracture toughness and shear behavior of composite bonded joints based on a novel aerospace adhesive. Composites Part B: Engineering 2012;43(2):240–8.
[10] Kim WS, Yun IH, Lee JJ, Jung HT. Evaluation of mechanical interlock effect on adhesion strength of polymer–metal interfaces using micro-patterned surface topography. International Journal of Adhesion and Adhesives 2010;30 (6):408–17.
[11] Molitor P, Barron V, Young T. Surface treatment of titanium for adhesive bonding to polymer composites: a review. International Journal of Adhesion and Adhesives 2001;21(2):129–36.

[12] Renton WJ, Vinson JR. The efficient design of adhesive bonded joints. Journal of Adhesion 1975;7(3):175–93.

[13] Da Silva LF, Adams R. Adhesive joints at high and low temperatures using similar and dissimilar adherends and dual adhesives. International Journal of Adhesion and Adhesives 2007;27(3):216–26.

[14] Zeng QG, Sun C. Novel design of a bonded lap joint. AIAA Journal 2001;39 (10):1991–6.

[15] Avila AF, Bueno PO. Stress analysis on a wavy-lap bonded joint for composites. International Journal of Adhesion and Adhesives 2004;24(5):407–14.

[16] Shiva Shankar GS, Vijayarangan S, Krishna NS. Failure analysis of lap and wavy-lap composite bonded joints. In: Proceedings of the international symposium of research students on materials science and engineering; 2004.

[17] Ashrafi M, Ajdari A, Rahbar N, Papadopoulos J, Nayeb-Hashemi H, Vaziri A. Adhesively bonded single lap joints with non-flat interfaces. International Journal of Adhesion and Adhesives 2012;32:46–52.

[18] Vaziri A, Nayeb-Hashemi H, Hamidzadeh H. Experimental and analytical investigations of the dynamic response of adhesively bonded single lap joints. Journal of Vibration and Acoustics 2004;126(1):84–91.

[19] Olia M, Rossettos J. Analysis of adhesively bonded joints with gaps subjected to bending. International Journal of Solids and Structures 1996;33(18):2681–93.

[20] Rossettos J, Zang E. On the peak shear stresses in adhesive joints with voids. NASA; 1997 [19990018176].

[21] Harris J, Adams R. Strength prediction of bonded single lap joints by non-linear finite element methods. International Journal of Adhesion and Adhesives 1984;4(2):65–78.

[22] Her SC. Stress analysis of adhesively-bonded lap joints. Composite Structures 1999;47(1):673–8.

[23] Vaziri A, Nayeb-Hashemi H. Dynamic response of tubular joints with an annular void subjected to a harmonic axial load. International Journal of Adhesion and Adhesives 2002;22(5):367–73.

[24] Benyus JM. Biomimicry: innovation inspired by nature. New York: William Morrow Paperbacks; 2002.

[25] Lenau T, Barfoed M. Material innovation–inspired by nature. Dansk Metallurgisk Selskab: Vintermødet; 2007. Byggecentrum Middelfart, p. 103–12.

[26] Barthelat F, Espinosa H. An experimental investigation of deformation and fracture of nacre–mother of pearl. Experimental Mechanics 2007;47 (3):311–24.

[27] Barthelat F, Tang H, Zavattieri PD, Li CM, Espinosa HD. On the mechanics of mother-of-pearl: a key feature in the material hierarchical structure. Journal of the Mechanics and Physics of Solids 2007;55(2):306–37.

[28] Katti KS, Katti DR, Pradhan SM, Bhosle A. Platelet interlocks are the key to toughness and strength in nacre. Journal of Materials Research 2005;20 (05):1097–100.

[29] Tang Z, Kotov NA, Magonov S, Ozturk B. Nanostructured artificial nacre. Nature Materials 2003;2(6):413–8.

[30] Phelps JB, Hubbard GB, Wang X, Agrawal CM. Microstructural heterogeneity and the fracture toughness of bone. Journal of Biomedical Materials Research 2000;51(4):735–41.

[31] Vashishth D. Rising crack-growth-resistance behavior in cortical bone:: implications for toughness measurements. Journal of Biomechanics 2004;37 (6):943–6.

[32] Ajdari A, Jahromi BH, Papdopoulos J, Nayeb-Hashemi H, Vaziri A. Hierarchical honeycombs with tailorable properties. International Journal of Solids and Structures 2012;49(11–12):1413–9.

[33] Haghpanah B, Oftadeh R, Papadopoulos J, Vaziri A. Self-similar hierarchical honeycombs, 469 (2156), 2013.

[34] Haghpanah B, Papadopoulos J, Vaziri A. Plastic collapse of lattice structures under a general stress state. Mechanics of Materials, 2013 (available online).

[35] Ajdari A, Nayeb-Hashemi H, Vaziri A. Dynamic crushing and energy absorption of regular, irregular and functionally graded cellular structures. International Journal of Solids and Structures 2011;48(3):506–16.

[36] Cui L, Kiernan S, Gilchrist MD. Designing the energy absorption capacity of functionally graded foam materials. Materials Science and Engineering: A 2009;507(1–2):215–25.

[37] Shim J, Perdigou C, Chen ER, Bertoldi K, Reis PM. Buckling-induced encapsulation of structured elastic shells under pressure. Proceedings of the National Academy of Sciences 2012;109(16):5978–83.